RSC Advances

PAPER

View Article Online
View Journal | View Issue



Cite this: *RSC Adv.*, 2020, **10**, 5116

# Nano ferrites ($AFe_2O_4$, A = Zn, Co, Mn, Cu) as efficient catalysts for catalytic ozonation of toluene†

Hongbin Jiang, Xiaochen Xu, * Rao Zhang, Yun Zhang,* Jie Chen and Fenglin Yang

Nano ferrites ($AFe_2O_4$, A = Zn, Co, Mn, Cu) were supported on the surface of γ-$Al_2O_3$ support by hydrothermal synthesis to prepare a series of novel composite catalysts ($AFe_2O_4$/γ-$Al_2O_3$) for catalytic ozonation for elimination of high concentration toluene at ambient temperature. The characterization results showed that the high-purity nano-$AFe_2O_4$ particles were uniformly loaded on mesoporous γ-$Al_2O_3$. Further, it was confirmed that among the several catalysts prepared, the amount of oxygen vacancies ($O_{vs}$), Lewis acid sites (LAS), and Brønsted acid sites (BAS) of the $ZnFe_2O_4$/γ-$Al_2O_3$ catalyst were the highest. This meant that the $ZnFe_2O_4$/γ-$Al_2O_3$ catalyst had a strong adsorption capacity for toluene and ozone ($O_3$), and had a strong catalytic activity. When the temperature was 293 K and the space velocity was 1500 $h^{-1}$, the mol ratio of $O_3$ to toluene was 6, the degradation rate of toluene (600 mg $m^{-3}$) can reach an optimum of 99.8%. The results of electron paramagnetic resonance (EPR) and Fourier infrared (FT-IR) proved superoxide radicals and hydroxyl radicals by catalytic ozonation. Moreover, the GC-MS analysis results indicated that the toluene degradation began with the oxidation of methyl groups on the benzene ring, eventually producing $CO_2$ and $H_2O$. After repeated experiments, the toluene degradation rate remained stable, and the residual content of $O_3$ in each litre of produced gas was less than 1 mg $L^{-1}$, thereby indicating that the $ZnFe_2O_4$/γ-$Al_2O_3$ catalyst had excellent reusability and showed great potential for the treatment of toluene waste gas.

Received 16th December 2019
Accepted 21st January 2020

DOI: 10.1039/c9ra10601d

rsc.li/rsc-advances



## Introduction

As a volatile organic compound (VOC), toluene, which has large emissions from industrial production,[1] has a certain carcinogenic effect and is capable of anaesthetizing the central nervous system.[2] Therefore, the management of toluene pollution is related to the health of all human beings. There are two broad categories of techniques to remove toluene: recycling processes and degradation processes. The recovery process includes adsorption[3] and condensation. Since the recovery method only enriches the pollutants and does not degrade them, it is usually not used for the treatment of high concentrations of toluene. The degradation processes include biological degradation,[4] photocatalysis,[5] catalytic combustion,[6] plasma catalytic degradation[7] and some emerging combined processes.[8] The degradation process can degrade toluene into environmentally friendly products, thereby avoiding the toluene re-contamination in the environment. At present, there are still some problems with most toluene degradation methods. The removal of toluene by biodegradation requires a very long reaction time (nearly 24 hours), and the degradation rate can only reach 80%.[9] Plasma catalytic degradation is a method of reaction under ambient temperature and pressure, but the discharge phenomenon during the reaction process may produce risks to its practical application.[8] Moreover, it is not suitable for a rapid removal of high concentration pollutants. Catalytic combustion is an efficient toluene treatment process, but it requires a large amount of energy consumption,[6] which causes higher costs.

$O_3$ is a highly effective oxidant without harmful by-products. However, the sole ozone oxidation has limited catalytic degradation capabilities.[10–12] Catalytic ozonation process can rapidly decompose $O_3$ into reactive oxygen species (ROS) with a higher oxidizing ability (*e.g.*, hydroxyl radicals, superoxide radicals, and so on) by the action of a catalyst at ambient temperature and pressure.[13] In addition, catalytic ozonation process also has the advantages of low operating cost, no secondary pollution, and low safety hazards. Therefore, catalytic ozonation process has received increasing attention and has been applied to control gaseous pollution in recent years. Kwong and Chao compared the effects of different zeolites and MCM-41 materials to remove toluene in catalytic ozonation process.[14] They found that the decomposition process of ozone was divided into

*Key Laboratory of Industrial Ecology and Environmental Engineering, Ministry of Education, School of Environmental Science and Technology, Dalian University of Technology, Linggong Road 2#, Dalian 116024, China. E-mail: xxcep@dlut.edu.cn; zhangyun@dlut.edu.cn; Fax: +86 411 84706328; Tel: +86 411 84706328*

† Electronic supplementary information (ESI) available. See DOI: 10.1039/c9ra10601d

two processes: adsorbed on the catalyst surface, and then decomposed into oxygen or active substances. Park *et al.* applied mesoporous $Mn/Al_2O_3$ catalyst to the process of catalyzing ozonation to degrade toluene at ambient temperature. The results indicated that some properties in metal oxides were essential to improve catalytic activity.[15] However, in the field of degrading VOC, catalyst research for catalytic ozonation is not optimistic. Most catalysts do not achieve the desired removal efficiency (less than 80%) at ambient temperatures.

For the catalytic ozonation process, it is especial to develop catalysts with higher activity and fewer by-products. For instance, mono or mixed metal oxides, supported metals and metal-free materials have been reported to be effective catalysts in accelerating ozone decomposition to generate reactive radicals. Recently, nanoscale ferrites ($AFe_2O_4$ (A = Zn, Co, Mn, Cu)) have received particular attention due to their low synthesis cost and better recyclability. Not only that, due to the diversity of elements and valence states in $AFe_2O_4$, surface defects are easily formed, making $AFe_2O_4$ have good catalytic activity. This will also greatly reduce the operating costs of catalytic degradation of pollutants. Such properties have demonstrated that they had good application prospects in environmental pollution control field.[16] Studies have confirmed that spinel ferrite had good catalytic activity in the ozonation of various pollutants. Therefore, $AFe_2O_4$ can be used as excellent ozonation catalysts for catalytic ozonation. Supported catalysts can improve the adsorption capacity and service life of the catalyst. In recent years, a variety of supports have been applied in the catalytic ozonation process. Catalytic ozonation is assumed to take place not only in the gaseous phase, but also on all the interfaces involved between the different phases. The adsorption of at least one reagent turns out to be an essential requirement for the surface reaction and the formation of ROS. Although there is no unified statement about the reaction mechanism's participation in the catalytic ozonation reaction, $\gamma$-$Al_2O_3$ is still one of the most commonly used catalyst supports in the research of catalytic ozonation due to its large surface area, low cost and modest chemical activity.[17]

Herein, the mesoporous alumina-supported $AFe_2O_4$ ($AFe_2O_4$/$\gamma$-$Al_2O_3$) were facilely synthesized by the hydrothermal reaction. The microstructure, morphology and composition of synthesized $AFe_2O_4/\gamma$-$Al_2O_3$ catalysts were investigated by a scanning electron microscope (SEM), Brunauer–Emmett–Teller (BET), X-ray diffraction (XRD), X-ray photoelectron spectroscopy (XPS). The active sites of the catalyst surface were studied by electron paramagnetic resonance (EPR) and pyridine-FTIR (Py-IR). Toluene, commonly found in both residential and industrial processes, was selected as model pollutant to evaluate the catalytic activity of $AFe_2O_4/\gamma$-$Al_2O_3$ catalysts at ambient temperature, and the optimal catalyst was selected for the reaction mechanism. A Fourier infrared spectrometer (FT-IR) and EPR were used to investigate the generation of the catalyst's surface-active factors and changes in adsorbed species during the reaction. Finally, the degradation intermediates were detected by GC-MS in the reaction process and the degradation pathway of toluene was summarized. To the best of the authors' knowledge, $AFe_2O_4/\gamma$-$Al_2O_3$ has not been reported as catalysts for removal of toluene in catalytic ozonation process.

## Experimental section

### Preparation of $AFe_2O_4/\gamma$-$Al_2O_3$ catalysts

A schematic illustration of the synthesis of $AFe_2O_4/\gamma$-$Al_2O_3$ is shown in Fig. S1.† The purchased mesoporous $\gamma$-$Al_2O_3$, at a size of 2–3 mm, washed with deionized water and dried in a constant temperature drying oven. A mixed solution of 0.1 mol $L^{-1}$ $Fe(NO_3)_3$ and 0.05 mol $L^{-1}$ $A(NO_3)_x$ was disposed. The pH of the solution was adjusted to 12–13 with an NaOH solution. Stirring continued for 30 min to completely precipitate the metal ions and obtain a reddish-brown precipitate. 200 g of the pre-treated $\gamma$-$Al_2O_3$ support was weighed into the mixed solution ultrasonically for 15 min at 300 W power. The mixture was placed in a 200 mL stainless steel autoclave lined with polytetrafluoroethylene, heated at 180 °C for 6 h, cooled and rinsed with deionized water. The product was air-dried at 80 °C for 6 h to obtain the $AFe_2O_4/\gamma$-$Al_2O_3$ catalysts. The mixed solution of 0.1 mol $L^{-1}$ $Fe(NO_3)_3$ and 0.05 mol $L^{-1}$ $A(NO_3)_x$ was replaced with 0.1 mol $L^{-1}$ $Fe(NO_3)_3$ solution and the above operation was repeated, the $Fe_2O_3/\gamma$-$Al_2O_3$ catalyst was obtained used as a control group for the $AFe_2O_4/\gamma$-$Al_2O_3$ catalysts in subsequent studies.

### Characterization

The surface morphology was examined using a scanning electron microscope (NOVA Nano SEM 450) equipped with an energy dispersive X-ray spectroscopy (EDS) detector. The specific surface area (BET) was estimated from the $N_2$ adsorption/desorption isotherm at −196 °C by using a Quantachrome SI gas sorption analyser. XRD is mainly used for the analysis of the crystal structure of materials. The test instrument model was Rigaku D/MAX-2400 powder diffractometer, using nickel-filtered copper radiation (CuK$\alpha$, $\lambda$ = 1.5406 Å) as a monochromatic, monochromatic detector was 40 kV, and at $2\theta$ range of 10–80°, respectively. XPS is used to characterize the surface element content of the material and its presence. The test instrument was Thermo Scientific's ESCALAB 250 device, and the device used an Al-K$\alpha$ target (photon energy of 1486.6 eV). The obtained spectrum was corrected by using the signal for the carbon peak (C 1s) at 284.5 eV. Acidity properties was investigated by Py-FTIR using a Thermo Nicolet 380 FT-IR analyzer under vacuum. EPR spectroscopy was measured at ambient temperature by Bruker ELEXSYS E500 X-band (~9.8 GHz) spectrometer. FTIR spectra were obtained by using a spectrometer (EQUINOX55) at a 4 $cm^{-1}$ resolution with scanning from 4000 to 400 $cm^{-1}$.

### Evaluation of catalytic activity

The schematic diagram of the experimental apparatus for catalytic ozonation toluene is shown in Fig. 1. The entire device included an intake system, a reaction system, and an analysis and detection system. First, the toluene and oxygen required for the reaction were supplied from the cylinder; subsequently,

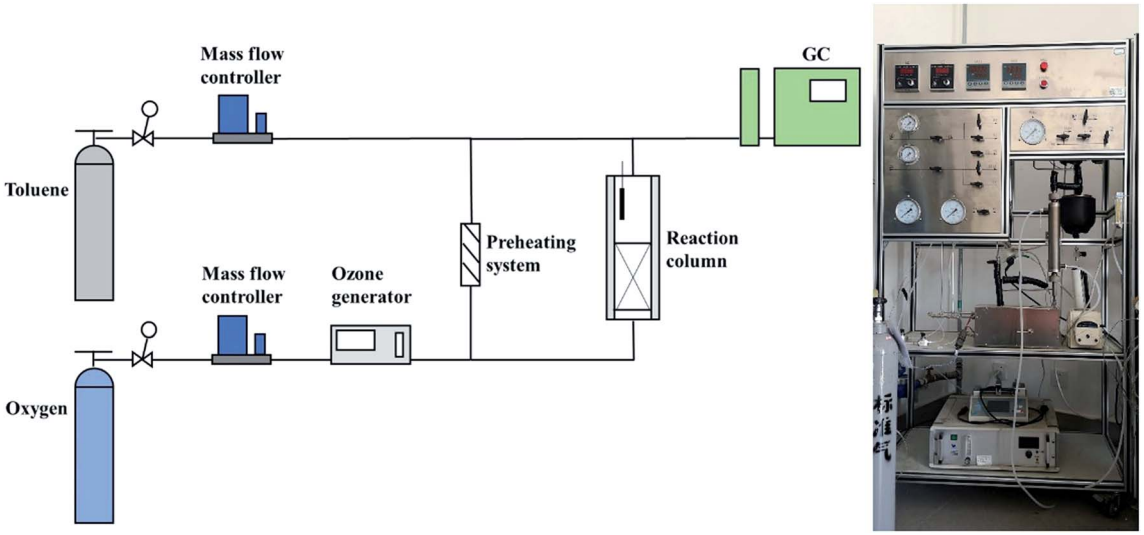


Fig. 1 Experimental setup for toluene catalytic ozonation.

oxygen was partially converted into $O_3$ by the $O_3$ generator and entered the reaction column together with the preheated toluene. During the reaction process, the toluene concentration, mass flow controller, and toluene preheating system were adjusted to control the toluene concentration, space velocity, and reaction temperature. The $O_3$ concentration was detected by $O_3$ concentration detectors at the inlet and outlet ends. Finally, the toluene concentration was monitored continually by gas chromatography (SHIMADZU GC-2010), and the toluene degradation rate was calculated by eqn (1):

$$\text{Toluene degradation rate} = 100\% \times (C_{in} - C_{out})/C_{in} \quad (1)$$

All data provided herein were averages obtained from three replicate experiment.

## Results and discussion

### Catalysts characterization

The surface morphologies of the support and the catalyst were observed using the scanning electron microscope (SEM). As shown in Fig. 2a, $\gamma$-$Al_2O_3$, which was used as the support, was porous with an irregular surface. In Fig. 2b–e, after the hydrothermal reaction, many rod-shaped nanoparticles appeared uniformly in the pores of $\gamma$-$Al_2O_3$. This structure was very similar to the rod-shaped ferrites particles.[18] The EDS element analysis in Fig. S2† showed that $AFe_2O_4/\gamma$-$Al_2O_3$ catalysts had relatively homogeneous distributions of Fe and other elements, and no contaminated elements were detected. The elemental compositions of Fe and other elements *via* EDS analysis confirmed that the atomic percentage of Fe and other elements was close to 2 : 1, which was consistent with the atomic composition of ferrite.

Fig. 2f–j illustrated the characterization of BET and Fig. S3–S7† showed the pore size distribution. In the characterization of BET, all samples showed an isotherm belonging to the mesoporous structure (type IV of the hysteresis loop of $H_3$).[19] The hysteresis loop of $\gamma$-$Al_2O_3$ described a wide morphology in the range of 0.40–1.00 relative pressure ($P/P_0$), while shrinks of $AFe_2O_4/\gamma$-$Al_2O_3$ catalysts were slightly smaller, denoting less structure. This conclusion was consistent with the phenomenon that the pore volume of $\gamma$-$Al_2O_3$ in Table S1† was reduced after loading. We can also observe that in Table S1,† compared with the $\gamma$-$Al_2O_3$, the specific surface area of $AFe_2O_4/\gamma$-$Al_2O_3$ catalysts was slightly lower and the average pore diameter was slightly higher. This was mainly due to the nano-ferrite particles entering the mesoporous $\gamma$-$Al_2O_3$ pores in the hydrothermal reaction, which caused partial pore plugging, and thereby the specific surface area and pore volume of the $\gamma$-$Al_2O_3$ after the load were reduced. This indicated that nano-ferrite particles were successfully loaded onto the mesoporous $\gamma$-$Al_2O_3$. At the same time, because the nano-ferrite particles blocked a part of the micropores, the average pore diameter of the mesoporous $\gamma$-$Al_2O_3$ after loading slightly increased. Among these $AFe_2O_4/\gamma$-$Al_2O_3$ catalysts, the $ZnFe_2O_4/\gamma$-$Al_2O_3$ catalyst had a large specific surface area, and it was estimated that it had a good ability in the field of adsorption and catalysis.

XRD was used to investigate the crystalline structure of the $\gamma$-$Al_2O_3$ support, $Fe_2O_3/\gamma$-$Al_2O_3$ catalyst and $AFe_2O_4/\gamma$-$Al_2O_3$ catalysts. As seen from Fig. 3, the three main characteristic peaks located *ca.* 35.60, 45.80 and 67.00 were observed for the $\gamma$-$Al_2O_3$, which may be primarily due to the crystalline phase of $\gamma$-$Al_2O_3$.[20] In spectra (e), the signal peaks at 30.28, 43.16, and 57.16 were characteristic peaks belonging to $Fe_2O_3/\gamma$-$Al_2O_3$. The XRD pattern of $AFe_2O_4/\gamma$-$Al_2O_3$ catalysts showed several characteristic diffraction peaks attributed to the (111), (200), (220), (311), (222), (400), (331), (420), (422) crystalline phase of the cubic fluorite structure. And the XRD pattern of $AFe_2O_4/\gamma$-$Al_2O_3$ catalysts indicated characteristic peaks, including $\gamma$-$Al_2O_3$ and ferrite. These results indicated that the high-purity ferrite was loaded on the $\gamma$-$Al_2O_3$ support successfully *via* hydrothermal synthesis.

 

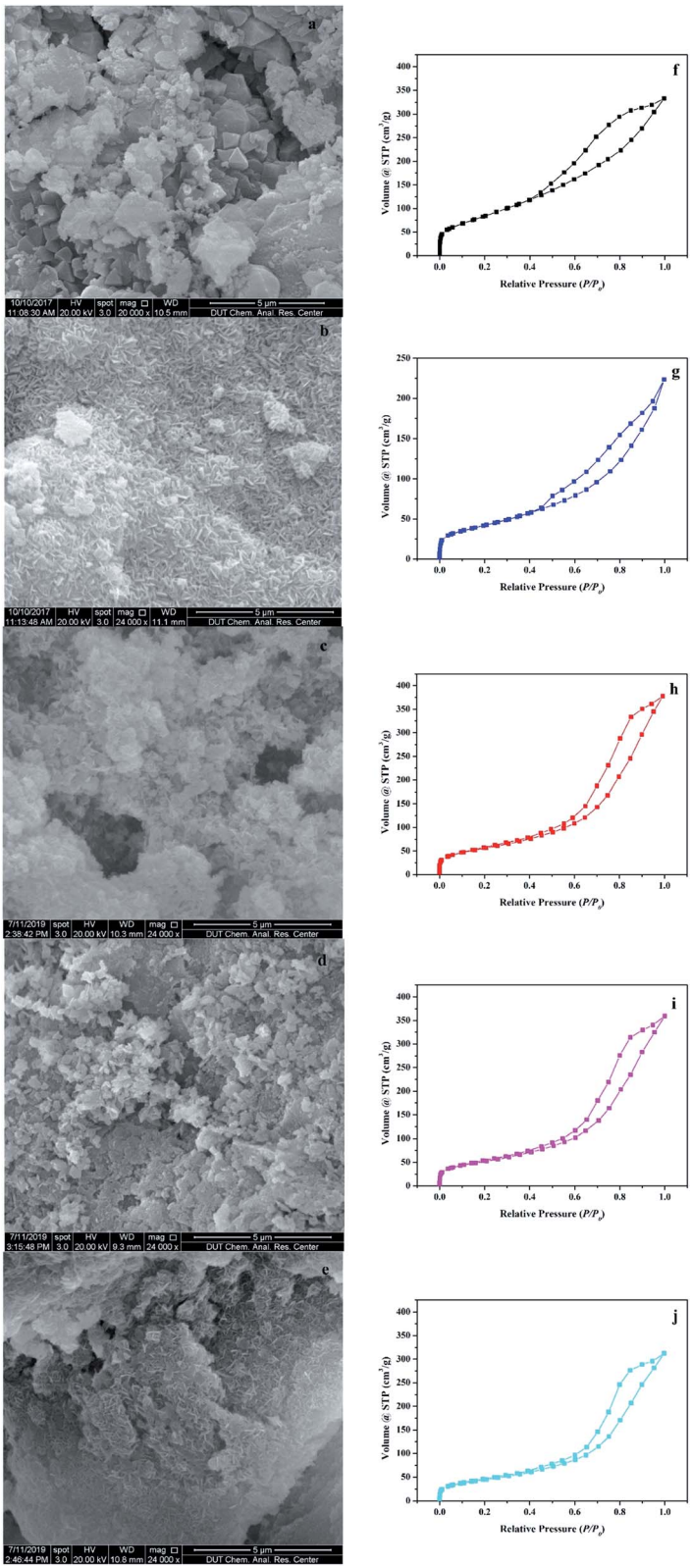


Fig. 2 SEM images of (a) $\gamma$-$Al_2O_3$, (b) $ZnFe_2O_4$/$\gamma$-$Al_2O_3$, (c) $CoFe_2O_4$/$\gamma$-$Al_2O_3$, (d) $MnFe_2O_4$/$\gamma$-$Al_2O_3$, and (e) $CuFe_2O_4$/$\gamma$-$Al_2O_3$, BET of (f) $\gamma$-$Al_2O_3$, (g) $ZnFe_2O_4$/$\gamma$-$Al_2O_3$, (h) $CoFe_2O_4$/$\gamma$-$Al_2O_3$, (i) $MnFe_2O_4$/$\gamma$-$Al_2O_3$, and (j) $CuFe_2O_4$/$\gamma$-$Al_2O_3$, respectively.

Further, we studied the composition of the catalyst surface chemical, XPS measurement was performed. As shown in Fig. S8a,† the presence of Zn at 1044.9 and 1022.5 eV can be attributed to Zn $2p_{1/2}$ and Zn $2p_{3/2}$ of $Zn^{2+}$ in $ZnFe_2O_4$, respectively. Fig. S8b† exhibits two peaks of 779.2 eV and 794.9 eV to binding energy of Mn $2p_{3/2}$ and Mn $2p_{1/2}$ respectively. Two

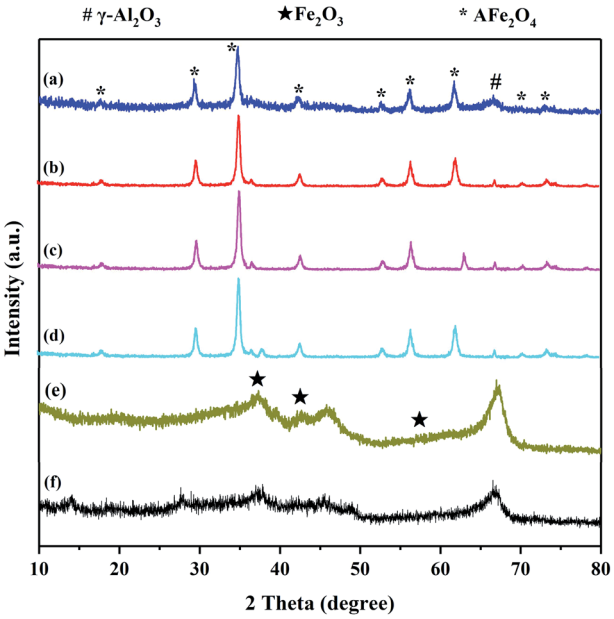


Fig. 3 XRD pattern of (a) $ZnFe_2O_4/\gamma\text{-}Al_2O_3$, (b) $CoFe_2O_4/\gamma\text{-}Al_2O_3$, (c) $MnFe_2O_4/\gamma\text{-}Al_2O_3$, (d) $CuFe_2O_4/\gamma\text{-}Al_2O_3$, (e) $Fe_2O_3/\gamma\text{-}Al_2O_3$ and (f) $\gamma\text{-}Al_2O_3$.

characteristic peaks in Fig. S8c† centred *ca.* 641.8 and 651.4 eV, respectively, are attributed to Mn $2p_{3/2}$ and Mn $2p_{1/2}$. In the Fig. S8d,† the BE of Cu 2p photoelectron peak was observed at 953.3 eV and 933.4 eV represented Cu $2p_{1/2}$ and Cu $2p_{3/2}$, respectively.[21,22] This again proved that the high-purity ferrite can be supported on $\gamma\text{-}Al_2O_3$ by the hydrothermal method of this study, consistent with the results of XRD.

Fig. 4a shows the Fe 2p spectra of $Fe_2O_3/\gamma\text{-}Al_2O_3$ catalyst and $AFe_2O_4/\gamma\text{-}Al_2O_3$ catalysts. In the spectra of $Fe_2O_3/\gamma\text{-}Al_2O_3$ catalyst, the characteristic peaks of Fe $2p_{3/2}$ and Fe $2p_{1/2}$ were located at 711.5 eV and 724.9 eV, respectively, which was consistent with the XPS spectra of $Fe_2O_3$ reported in the literature.[23] There was a tiny satellite peak around 720 eV, which was also a typical feature of $Fe_2O_3$. As the spectra of $AFe_2O_4/\gamma\text{-}Al_2O_3$ catalysts, there were some changes in the positions of Fe $2p_{3/2}$ and Fe $2p_{1/2}$ in different catalysts. It shows that there was electron exchange between Fe and other elements in the catalyst.[24] Combined with Table 1, the XPS results of $AFe_2O_4/\gamma\text{-}Al_2O_3$ catalysts were displayed that Fe/A $\approx$ 2 was similar to the EDS result. The Fe $2p_{3/2}$ peak was deconvoluted into two peaks with binding energies at 709 and 713 eV, corresponding to $Fe^{2+}$ and $Fe^{3+}$, respectively,[25,26] whose ratios are summarized in Table 1. The $ZnFe_2O_4/\gamma\text{-}Al_2O_3$ catalyst had a relatively high proportion of $Fe^{2+}$ on its surface. The proportion of the low-valent state of the modifying element in the transition metal oxide is closely related to the generation of $O_{vs}$.[27] In this study, the change of the iron element from $Fe^{3+}$ to $Fe^{2+}$ indirectly represented the $O_{vs}$ introduced into the crystal lattice. The $O_{vs}$ on the surface of the catalyst can promote the decomposition of $O_3$ to produce more oxidizing active substances.[28]

The corresponding O 1s spectrum of $\gamma\text{-}Al_2O_3$ and $AFe_2O_4/\gamma\text{-}Al_2O_3$ catalysts in Fig. 4b can be deconvoluted into two distinct peaks: surface oxygen (expressed as $O_\alpha$) at 528.4–530.5 eV, and lattice oxygen (expressed as $O_\beta$) at 526.7–527.9 eV, respectively.[29,30] Combined with Table 1, we observed that the proportion of $O_\alpha$ in the $ZnFe_2O_4/\gamma\text{-}Al_2O_3$ catalyst, the $CoFe_2O_4/\gamma\text{-}Al_2O_3$ catalyst and the $CuFe_2O_4/\gamma\text{-}Al_2O_3$ catalyst were increased compared to $\gamma\text{-}Al_2O_3$, while the $ZnFe_2O_4/\gamma\text{-}Al_2O_3$ catalyst was the most. Since $O_\alpha$ was provided by an electrostatically charged substance such as $H_2O$, ·OH on surface of the catalyst, the higher the proportion of $O_\alpha$ in the oxygen element distribution, the stronger the adsorption performance of the catalyst on the $O_3$.[31] In the gas phase catalytic ozonation reaction, a high adsorption capacity for $O_3$ was a guarantee of high catalytic efficiency. This indicated that the adsorption capacity of $\gamma\text{-}Al_2O_3$ for $O_3$ was improved by addition of $ZnFe_2O_4$, which provided a foundation for improving the catalytic efficiency.

In order to further determine the type and amount of $AFe_2O_4/\gamma\text{-}Al_2O_3$ catalysts surface active sites, we carried out EPR and pyridine infrared tests on $\gamma\text{-}Al_2O_3$ and $AFe_2O_4/\gamma\text{-}Al_2O_3$ catalysts without illumination. From Fig. 5a, we observed that all samples had obvious signal peaks belonging to $O_{vs}$ at $g$ = 2.004.[32] Notably, the signal intensity of the $\gamma\text{-}Al_2O_3$ was significantly lower than that of $ZnFe_2O_4/\gamma\text{-}Al_2O_3$ catalyst, the $CoFe_2O_4/\gamma\text{-}Al_2O_3$ catalyst and the $CuFe_2O_4/\gamma\text{-}Al_2O_3$ catalyst. It showed that the amount of $O_{vs}$ on the surface of these catalysts was higher than that of alumina carriers, which was consistent with our speculation through XPS results. This indicated that the introduction of suitable ferrite could increase the amount of $O_{vs}$ on the $\gamma\text{-}Al_2O_3$ surface.

In the Py-FTIR test, we used the signal intensity of pyridine at 150 °C to measure the amount of LAS and BAS on the surfaces of $\gamma\text{-}Al_2O_3$ and $AFe_2O_4/\gamma\text{-}Al_2O_3$ catalysts. Fig. 5b clearly showed that both the amount of LAS and BAS had a certain degree of change after loading. 1630 and 1546 $cm^{-1}$ were the desorption peaks after pyridine was adsorbed to BAS; 1612 and 1458 $cm^{-1}$ were the desorption peaks after pyridine was adsorbed to LAS; 1490 $cm^{-1}$ was pyridine adsorbed simultaneously at BAS and LAS desorption peak.[33] The amount and proportional relationship of each acidic site were summarized in Table S2.† Among all the samples, the $ZnFe_2O_4/\gamma\text{-}Al_2O_3$ catalyst showed the strongest L acidity and B acidity. Compared with $\gamma\text{-}Al_2O_3$, the acidity of other catalysts decreased, which may be due to the fact that the elements (such as Co, Mn and Cu) were more easily ion exchanged with protons in $\gamma\text{-}Al_2O_3$, so that the original acidic sites of $\gamma\text{-}Al_2O_3$ were consumed.[34] Previous studies have confirmed that both LAS and BAS had an adsorption effect on weakly basic aromatic hydrocarbon VOCs molecules such as toluene.[35] Therefore, the adsorption capacity of the catalyst increased with the increase of the total amount of acidic sites. From this we could speculate that the $ZnFe_2O_4/\gamma\text{-}Al_2O_3$ catalyst had the best toluene adsorption capacity of all $AFe_2O_4/\gamma\text{-}Al_2O_3$ catalysts involved in this study.

### Catalytic ozonation for toluene degradation and life cycle of catalyst

In order to further study the catalytic performance of the catalyst in the catalytic ozonation degradation of toluene,

 

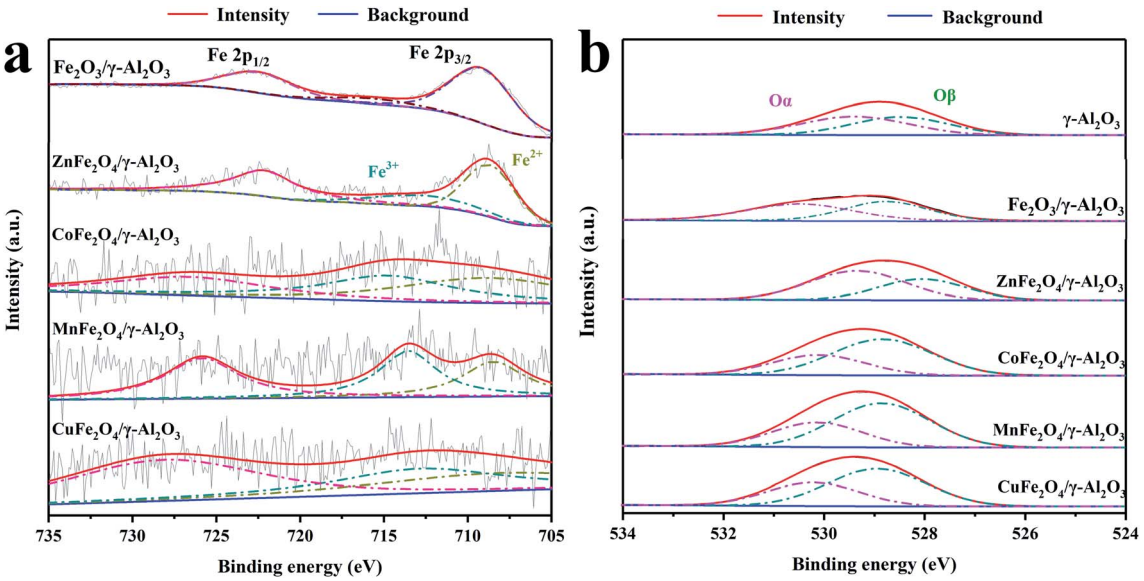


Fig. 4 XPS spectra of $AFe_2O_4/\gamma\text{-}Al_2O_3$ catalysts, (a) Fe 2p of $Fe_2O_3/\gamma\text{-}Al_2O_3$ catalyst and $AFe_2O_4/\gamma\text{-}Al_2O_3$ catalysts; (b) O 1s of $\gamma\text{-}Al_2O_3$, $Fe_2O_4/\gamma\text{-}Al_2O_3$ catalyst and $AFe_2O_4/\gamma\text{-}Al_2O_3$ catalysts.

adsorption and degradation experiments on toluene were carried out at a concentration of 600 mg $m^{-3}$. The experimental conditions were as follows: temperature 303 K and space velocity 2000 $h^{-1}$. As illustrated in Fig. 6a, the adsorption capacities of the $\gamma\text{-}Al_2O_3$ and $AFe_2O_4/\gamma\text{-}Al_2O_3$ catalysts for toluene were investigated when the $O_3$ concentration was 0 mg $L^{-1}$. All samples had relatively stable adsorptions to toluene, and the optimal adsorption efficiency was maintained above 6 h. The adsorption capacity of the $ZnFe_2O_4/\gamma\text{-}Al_2O_3$ catalyst was slightly better than $\gamma\text{-}Al_2O_3$ and other samples, which was consistent with the conclusion that the acidic site of the $ZnFe_2O_4/\gamma\text{-}Al_2O_3$ catalyst was higher and its adsorption capacity was better. The results confirmed that the $ZnFe_2O_4/\gamma\text{-}Al_2O_3$ catalyst had a high toluene adsorption capacity, and the toluene removal rate was only approximately 40%. Fig. 6b showed that the toluene removal efficiency of $\gamma\text{-}Al_2O_3$ and $AFe_2O_4/\gamma\text{-}Al_2O_3$ catalysts system increased significantly after the addition of $O_3$ and became larger with the increase in $O_3$ dosage. Among them, the toluene removal efficiency of the $ZnFe_2O_4/\gamma\text{-}Al_2O_3$ catalyst system exceeded 95% at most. However, despite the introduction of $O_3$, in the absence of any catalyst addition, the removal efficiency was still relatively low, and even lower than the removal efficiency of the catalyst adsorption. This result demonstrated that with the reaction conditions, $O_3$ did not have the ability to remove toluene efficiently. In summarizing these conclusions, we may deduce that the removal of the high concentration toluene by catalytic ozonation was a combination of adsorption and catalytic oxidation, rather than a separate adsorption or sole ozonation. The introduction of a suitable catalyst may effectively increase the efficiency of catalytic ozonation to remove toluene. The $ZnFe_2O_4/\gamma\text{-}Al_2O_3$ catalyst had a better adsorption capacity and better application prospects for catalytic ozonation.

To determine the oxidation kinetics of toluene in each process, the kinetic parameters of the oxidation process were investigated (the experimental conditions were as follows: temperature 293 K, space velocity 2000 $h^{-1}$, initial toluene concentration: 600 mg $m^{-3}$). Zero-order and pseudo first-order equations were used for fitting dynamic data.[36] Table S3† shows the fitting results of the toluene oxidation kinetic data for sole $O_3$, $\gamma\text{-}Al_2O_3$ and $AFe_2O_4/\gamma\text{-}Al_2O_3$ catalysts. Obviously, the correlation coefficients ($R^2$) of pseudo first-order kinetic were higher than the zero-order kinetics. Thence, pseudo first-order kinetics accurately described toluene-catalyzed ozonation. The reaction

Table 1 XPS results of $\gamma\text{-}Al_2O_3$ and $AFe_2O_4/\gamma\text{-}Al_2O_3$ catalysts

| | O (%) | Fe (%) | A (%) | $Fe^{2+}/(Fe^{2+}+Fe^{3+})$ (%) | $O_\alpha/(O_\alpha+O_\beta)$ (%) |
|---|---|---|---|---|---|
| $ZnFe_2O_4/\gamma\text{-}Al_2O_3$ catalyst | 46.57 | 0.88 | 0.43 | 70.2 | 52.5 |
| $CoFe_2O_4/\gamma\text{-}Al_2O_3$ catalyst | 46.83 | 0.83 | 0.43 | 52.1 | 37.6 |
| $MnFe_2O_4/\gamma\text{-}Al_2O_3$ catalyst | 47.64 | 0.39 | 0.22 | 44.8 | 34.1 |
| $CuFe_2O_4/\gamma\text{-}Al_2O_3$ catalyst | 47.37 | 0.42 | 0.18 | 47.6 | 36.9 |
| $Fe_2O_3/\gamma\text{-}Al_2O_3$ catalyst | 47.14 | 1.32 | | | 35.8 |
| $\gamma\text{-}Al_2O_3$ | 55.94 | | | | 36.2 |

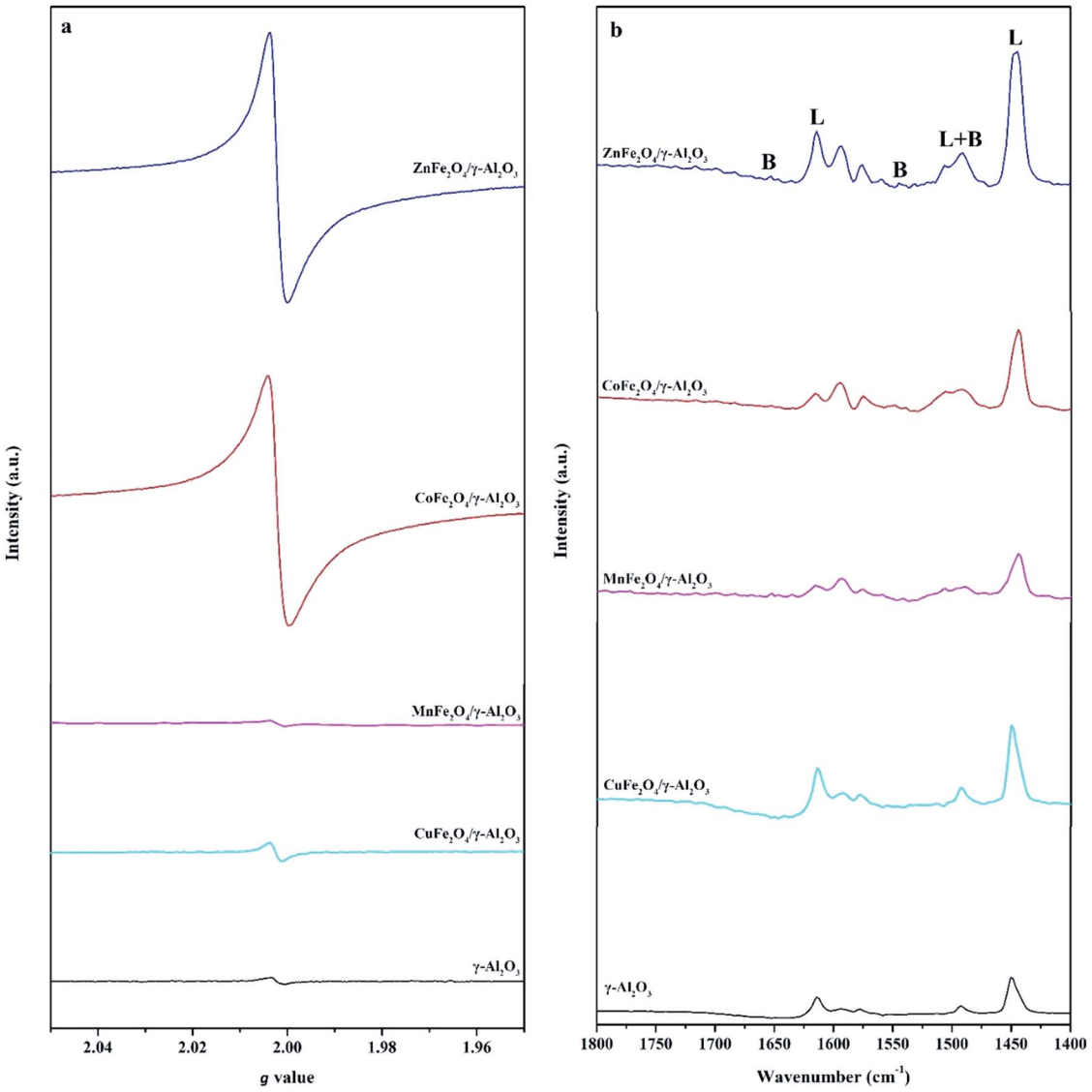


Fig. 5 (a) The EPR spectra of γ-$Al_2O_3$ and $AFe_2O_4$/γ-$Al_2O_3$ catalysts; (b) Py-FTIR spectra of γ-$Al_2O_3$ and $AFe_2O_4$/γ-$Al_2O_3$ catalysts after pyridine desorbed at 150 °C.

rate *k* of the other samples was lower than that of the $ZnFe_2O_4$/γ-$Al_2O_3$ catalyst, which proved that the $ZnFe_2O_4$/γ-$Al_2O_3$ catalyst had a higher catalytic efficiency.

Studies have investigated that the electronegativity of lower metal oxides led to higher reducing power. The electron density of the $O^{2-}$ bond combined with the metal will also become higher, which is beneficial to the decomposition of ozone into free radicals, due to the electrophilic properties of ozone.[37] The metallicity of Zn is higher than that of the fourth period transitional metals according to the standard redox potential order.[37] This indicates that $ZnFe_2O_4$ is a material with higher catalytic ozonation activity in ferrites, and our study also have confirmed this view through experiments.

After determining that the $ZnFe_2O_4$/γ-$Al_2O_3$ catalyst was the best catalyst, we investigated the optimum reaction conditions for toluene removal by catalytic ozonation with the $ZnFe_2O_4$/γ-$Al_2O_3$ catalyst.

Because the concentration of toluene in industrial waste gas was between 200–400 mg $m^{-3}$, we selected the toluene simulated waste gas with initial concentrations of 200, 400, 600 and 800 mg $m^{-3}$ for experimentation. The experimental conditions were as follows: temperature 303 K and space velocity 2000 $h^{-1}$. As shown in Fig. 6c, for an $O_3$ mol dosing ratio of 2, the catalytic ozonation process had a significant removal effect on toluene concentrations from 200 mg $m^{-3}$ to 800 mg $m^{-3}$. For toluene with a concentration greater than 400 mg $m^{-3}$, it could not be degraded efficiently when the $O_3$ mol dosing ratio was 1; the degradation rate was less than 80%. Subsequently, we increased the amount of $O_3$ added. Toluene at a concentration of 200 mg $m^{-3}$ quickly reached a degradation rate close to 100% and remained stable. For toluene with a concentration of 400–800 mg $m^{-3}$, the degradation rate showed a gradual positive correlation with the $O_3$ mol dosing ratio. When the $O_3$ mol dosing ratio reached 7, all concentrations achieved a high

 

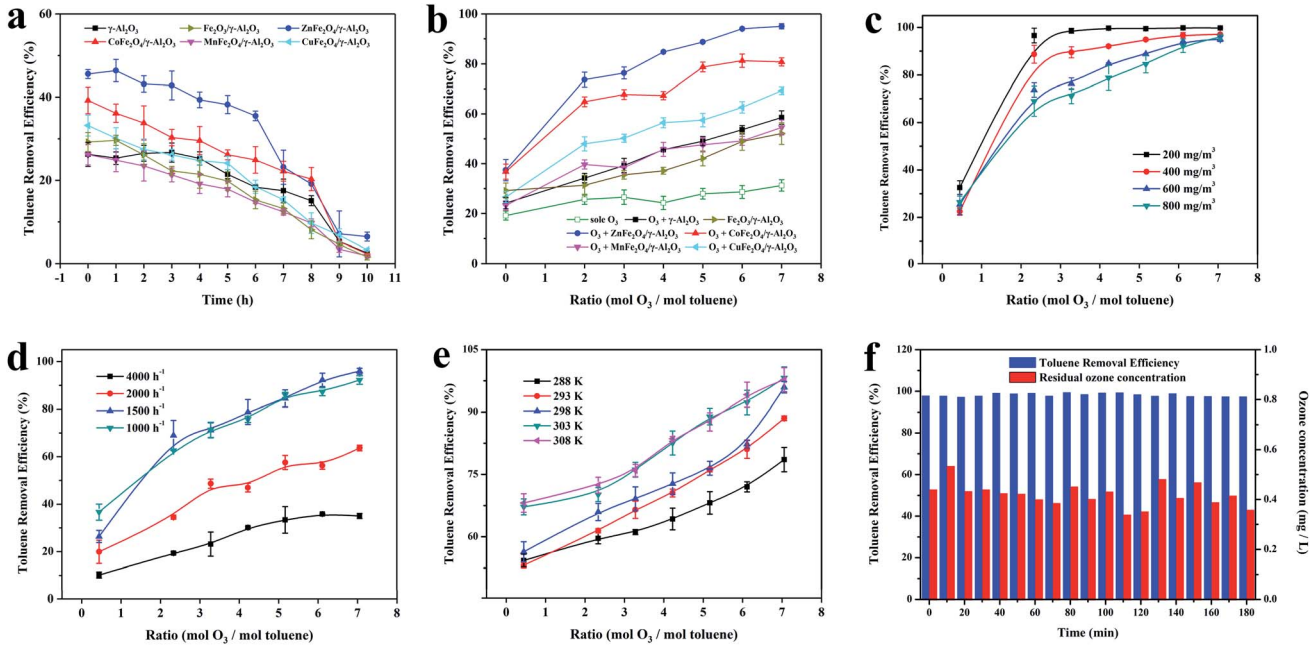


Fig. 6 (a) Adsorption efficiency of $\gamma$-$Al_2O_3$, $Fe_2O_3$/$\gamma$-$Al_2O_3$ catalyst and $AFe_2O_4$/$\gamma$-$Al_2O_3$ catalysts; (b) catalytic efficiency of $\gamma$-$Al_2O_3$, $Fe_2O_3$/$\gamma$-$Al_2O_3$ catalyst and $AFe_2O_4$/$\gamma$-$Al_2O_3$ catalysts; (c) removal of toluene at different initial toluene concentrations with $ZnFe_2O_4$/$\gamma$-$Al_2O_3$ catalyst; (d) removal of toluene at different space velocities with $ZnFe_2O_4$/$\gamma$-$Al_2O_3$ catalyst; (e) removal of toluene at different reaction temperatures with $ZnFe_2O_4$/$\gamma$-$Al_2O_3$ catalyst and (f) the variation law of toluene degradation rate in long-term test with $ZnFe_2O_4$/$\gamma$-$Al_2O_3$ catalyst.

degradation rate of nearly 100%. Combined with previously published studies,[11] the catalyst surface was speculated to be the site of $O_3$ decomposition and catalytic ozonation. Therefore, when the amount of toluene was too large, more $O_3$ was required to maintain the adsorption equilibrium on the catalysts. The experimental results also proved that the degradation rate gradually increased after the $O_3$ dosage improved.

At temperature 303 K and a toluene concentration of 600 mg $m^{-3}$, we summarized the effect of the space velocity on the catalytic reaction. The results are shown in Fig. 6d, with the same $O_3$ mol dosing ratio, the same trend occurred in the change of the toluene degradation rate. As the space velocity decreased, the toluene degradation rate increased. At a space velocity of 4000 $h^{-1}$, the degradation rate was lower at each $O_3$ mol ratio. When the space velocity was reduced to below 1500 $h^{-1}$, the toluene degradation rates no longer rose and remained stable. The reason for this experimental situation was that when the space velocity was large, the adsorption of toluene by the catalyst was limited, which limited the degradation ability of the catalytic ozonation process for toluene. When the space velocity was continuously reduced, the adsorption of toluene by the catalyst was gradually obvious, the degradation efficiency was significantly improved. The effect of the space velocity on the ability of the catalyst to adsorb toluene was also manifested when the $O_3$ dosage was 0 in Fig. 6d. In this condition, we also found that when the space velocity dropped below 1500 $h^{-1}$, the adsorption capacity of the catalyst for toluene still improved. This indicated that after the adsorption reached a certain intensity, the catalytic oxidation began to take the initiative and became the main way to remove toluene. With the same space velocity condition, the toluene degradation rate was positively correlated with the $O_3$ mol addition ratio, showing the same regularity as the previous experiment.

The optimum temperature for the reaction was the key to the engineering application of a process. The effect of temperature on the catalytic performance of the $ZnFe_2O_4$/$\gamma$-$Al_2O_3$ catalyst to 600 mg $m^{-3}$ toluene at a space velocity of 2000 $h^{-1}$ is shown in Fig. 6e. When the $O_3$ mol ratio was determined, the toluene degradation rate positively correlated with the reaction temperature. The toluene degradation rates at 303 K and 308 K were similar and higher than the other temperatures. On the other hand, with the introduction of $O_3$, the toluene degradation rate of each $O_3$ mol dosing ratio showed another kind of change law. From the two laws of change, the temperature affected not only the adsorption of toluene on the catalyst but also the efficiency of the catalytic ozonation. After the temperature reached 303 K, the removal efficiency of toluene greatly improved during the catalytic ozonation process.

As shown in previous studies, the catalytic ozonation reaction accords with the pseudo first-order kinetics. We kinetically fitted the removal efficiency of toluene at each temperature, and the results are shown in Fig. S9.† Combined with Table S4,† we concluded that the reaction rate $k$ of the catalytic ozonation positively correlated with temperature and tended to be stable after the temperature reached 303 K. This was consistent with our previous conclusions. By incorporating the data in Table S4† into the Arrhenius formula, the activation energy of the catalytic ozonation toluene of the $ZnFe_2O_4$/$\gamma$-$Al_2O_3$ catalyst was calculated to be 69.94 kJ $mol^{-1}$. High-quality catalysts must not only have a high catalytic efficiency but also have a long service

life. In this study, a long-term comparative experiment was conducted on the catalytic efficiency and residual $O_3$ concentration of the $ZnFe_2O_4/\gamma$-$Al_2O_3$ catalyst. The experimental conditions were as follows: temperature 293 K, space velocity 2000 $h^{-1}$, and an initial toluene concentration 600 mg $m^{-3}$.

As shown in Fig. 6f, with the reaction time prolonged, there was no significant decrease in the removal efficiency of toluene and the residual $O_3$ concentration. In this study, the introduction of the $ZnFe_2O_4/\gamma$-$Al_2O_3$ catalyst greatly improved the degradation ability of catalytic ozonation system to toluene, and the system obtained a stable high toluene removal efficiency and a suitable residual $O_3$ concentration. The $ZnFe_2O_4/\gamma$-$Al_2O_3$ catalyst was a catalytic ozonation process catalyst with a high efficiency and long active life.

### $O_3$ utilization efficiency

This study explored the $O_3$ decay during the $O_3$ and catalytic ozonation processes at different initial $O_3$ concentrations. To guarantee that the research has certain theoretical value, this section's methods were carried out under reasonable $O_3$ concentration conditions. According to a comprehensive published study, $O_3$ has a mass balance in a gas phase reaction and can be expressed as shown below:

$$[O_3]_t = [O_3]_w + [O_3]_s + [O_3]_u \quad (2)$$

$[O_3]_t$, $[O_3]_w$, $[O_3]_s$ and $[O_3]_u$ represent the concentrations of total $O_3$, wasted $O_3$ in the exhaust, surplus $O_3$ in the reaction column and the utilized $O_3$, respectively. So, $[O_3]_u$ can be expressed as:

$$[O_3]_u = [O_3]_t - [O_3]_w - [O_3]_s \quad (3)$$

According to the mass balance formula of $O_3$ eqn (3), the $O_3$ utilization efficiency ($R_u$%), which is considered as a primary indicator of catalyst performance, can be expressed as follows:

$$R_u\% = \frac{\int_0^t v_O[O_3]_t dt - \int_0^t (v_O + v_t)[O_3]_w dt - V[O_3]_s}{\int_0^t v[O_3]_t dt} \times 100 \quad (4)$$

where $v_O$ and $v_t$ are the flow rates of gas $O_3$ and gas toluene, respectively. $V$ is the reaction column volume. Subsequently, the amount of $O_3$ consumed to remove toluene by different process systems can be evaluated according to the following equation eqn (5):[38]

$$\eta = \frac{R_u \int_0^t v[O_3]_t dt}{\int_0^t v_t([\text{toluene}]_0 - [\text{toluene}]_t) dt} \quad (5)$$

Since $[O_3]_w$ and $[O_3]_s$ exist in a gas phase state in the reaction system, $[O_3]_s$ is approximately equal to $[O_3]_w$. In Table S5,† $[O_3]_w$ and $[O_3]_s$ in catalytic ozonation was lower than in the sole ozonation. This confirmed that more $O_3$ was rapidly decomposed for catalytic reaction in the presence of $\gamma$-$Al_2O_3$ and the $ZnFe_2O_4/\gamma$-$Al_2O_3$ catalyst ozonation than sole ozonation.

The evolution of the $R_u$ value in Fig. 7a indicated that compared with the sole ozonation and $\gamma$-$Al_2O_3$ ozonation processes, the catalytic ozonation process with the $ZnFe_2O_4/\gamma$-$Al_2O_3$ catalyst had a higher $R_u$ value, during $O_3$ concentrations of 5–20 mg $L^{-1}$. On the contrary, the change trend of the $\eta$ value was different. Fig. 7b clearly showed that the $\eta$ value of the $ZnFe_2O_4/\gamma$-$Al_2O_3$ ozonation processes was lower than the sole ozonation at each $O_3$ concentration interval, and was also slightly lower than $\gamma$-$Al_2O_3$ ozonation. This meaned that $O_3$ can effectively decompose and produce active substances with the help of the catalyst, and the $ZnFe_2O_4/\gamma$-$Al_2O_3$ catalyst had a higher $R_u$ value and a lower $\eta$ value. Compared to direct $O_3$ reaction and conventional catalytic ozonation, the degradation efficiency of toluene was greatly improved.

### The catalytic ozonation mechanism of toluene oxidation

Recent studies have demonstrated that $O_{vs}$ was a key role in catalytic ozonation systems. First, the $O_{vs}$ adsorbed $O_3$ on the catalyst surface by combining with an oxygen atom in the ozone molecule. Then, two electrons were transferred to the O atom, forming $\cdot O^-$ and $O_2$ (eqn (6)). The formed $\cdot O^-$ can react with another $O_3$ molecule to form $O_2$ and superoxide ($\cdot O_2^-$) (eqn (7)). Superoxide ($\cdot O_2^-$) can decompose and release oxygen vacancies and $O_2$ (eqn (8)), they may participate in the next $O_3$ decomposition cycle.[11,39,40] Therefore, as a reaction site, the $O_{vs}$ not only enhances the absorption of $O_3$ by the catalyst but also forms superoxide radicals with the $O_3$, thereby enhancing catalytic oxidation.

$$O_{vs} + O_3 \rightarrow O_2 + \cdot O^- \quad (6)$$

$$\cdot O^- + O_3 \rightarrow O_2 + \cdot O_2^- \quad (7)$$

$$\cdot O_2^- \rightarrow O_2 + O_{vs} \quad (8)$$

We investigated the catalytic ozonation process to degrade toluene according to the following reaction steps (eqn (9) and (10)). The reaction pathway for catalytic ozonation can be summarized as follows:[41]

$$O^* + \text{toluene} \rightarrow \text{intermediates; } CO_2 \text{ and } CO \quad (9)$$

$$\text{Intermediates and } CO + O_3 \text{ and } O^* \rightarrow H_2O + CO_2 \quad (10)$$

From eqn (9) and (10), we noticed that there was $H_2O$ generation in the degradation process of toluene. On the other hand, the $\cdot O_2^-$ also had the following reactions from eqn (11) in the presence of $H_2O$.[11] Based on these findings, we conclude that during the degradation of toluene, due to the formation of the $H_2O$ or humidity of the gas during the reaction, hydroxyl radicals ($\cdot OH$) are generated and participate in the degradation process. They can directly extract H atoms from toluene methyl groups to form benzyl groups, making subsequent degradation of toluene easier.[11]

$$\cdot O_2^- + H_2O \rightarrow 2 \cdot OH \quad (11)$$

 

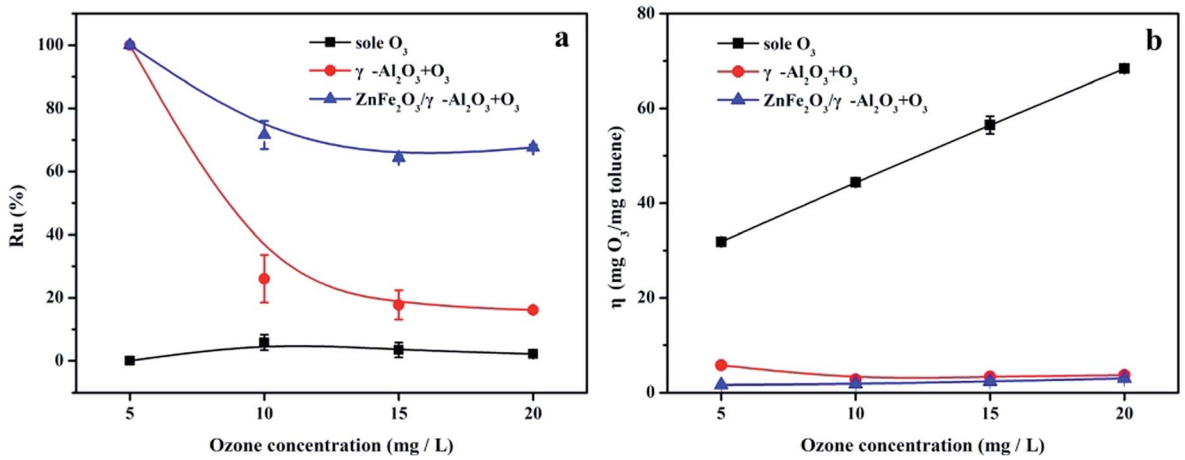


Fig. 7 (a) $R_u$% in sole ozonation and catalytic ozonation processes, respectively; (b) $\eta$ in sole ozonation and catalytic ozonation processes, respectively.

In this paper, the EPR DMPO spin trap technique was applied to verify the presence of radicals. According to the experimental conditions, the $O_3$ was continuously introduced into the mixed solution of the $ZnFe_2O_4$/γ-$Al_2O_3$ catalyst, 10 mL of liquid toluene and a 1 mM DMPO solution at ambient temperature with an space velocity of 2000 $h^{-1}$. The signals of $\cdot O_2^-$ and ·OH were observed as depicted in Fig. 8a.[41] From the analysis of EPR, the addition of $ZnFe_2O_4$ was beneficial to the production of radicals. The superoxide radicals and hydroxyl radicals had significantly higher oxidation rates than $O_3$ alone. Therefore, we concluded that the oxygen activity factor and ·OH generated during the reaction accelerated the degradation of toluene, which was in line with the abovementioned speculation about the degradation mechanism of toluene.

FT-IR was used to study the changes of adsorbed components during the degradation of the $ZnFe_2O_4$/γ-$Al_2O_3$ catalyst, and the reaction pathways were discussed. We performed FT-IR characterization of the catalyst before and after the degradation experiment, the results are shown in Fig. 8b. For two spectra, there were two distinctly characteristic peaks at 559 $cm^{-1}$ and 425 $cm^{-1}$, which were generally considered to be characteristic peaks of the infrared spectrum of the ferrite composite.[42] In the crystal structure, each oxygen atom was shared by one tetrahedral cation and three octahedral cations, so the vibration of $O_2^-$ was related to both the tetrahedron and octahedron, and the characteristic peak at 559 $cm^{-1}$ was tetrahedral Zn–O. And the characteristic peak of 425 $cm^{-1}$ was the vibration of a typical Fe–O bond.[43] The characteristic peaks found at 1638 $cm^{-1}$ and 3490 $cm^{-1}$ were derived from the surface hydroxyl groups of samples.[42] This finding was consistent with XPS analysis, where the catalyst surface contained a higher proportion of $O_\alpha$. After the oxidation reaction, the strength of the surface hydroxyl group was slightly reduced, thereby explaining that some $O_\alpha$ would participate or be temporarily covered during the reaction. After being used in the catalytic ozonation, the FT-IR spectrum showed a strong characteristic peak at 1381 $cm^{-1}$ after the

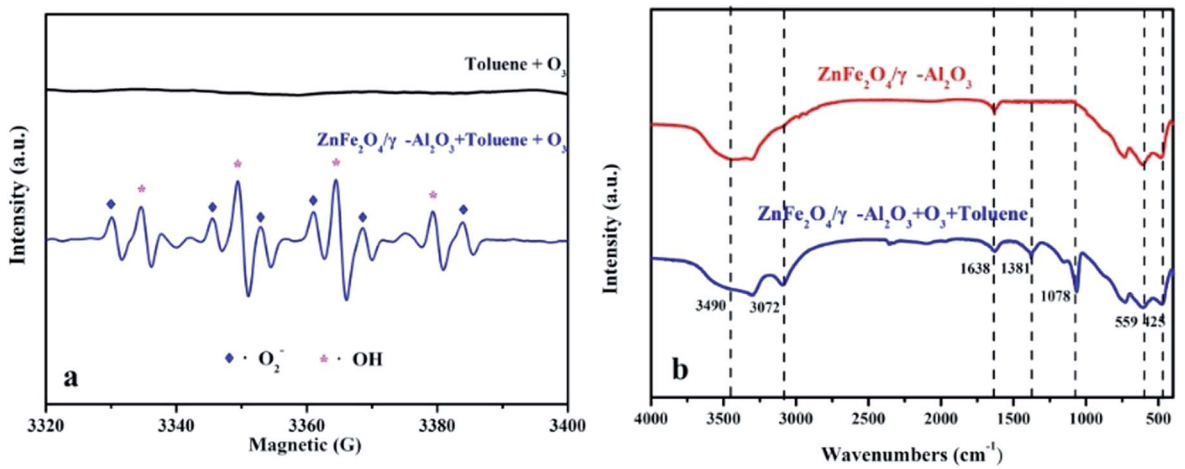


Fig. 8 (a) EPR spectra of superoxide radicals and hydroxyl radicals; (b) FT-IR spectra of γ-$Al_2O_3$ and $ZnFe_2O_4$/γ-$Al_2O_3$ catalyst in unozonation, after use in gaseous mixture of $O_3$ and toluene.

reaction. This characteristic peak was usually attributed to the surface oxide produced by the combination of $O_3$ and LAS.[44,45] This phenomenon confirmed the fact that both the $\gamma$-$Al_2O_3$ and the $ZnFe_2O_4/\gamma$-$Al_2O_3$ catalyst contained a certain amount of LAS in the Py-IR, and also indicated that the active site was not completely covered during the reaction. The active substance produced by the decomposition of $O_3$ was the key to catalyze the ozonation reaction. In referring to the relevant literature,[25,26] the reaction process of the catalyst surface during the reaction may be summarized as shown in Fig. S10.† We also observed that a characteristic peak appeared at 1078 $cm^{-1}$, which was the characteristic peak position belonging to C–O. We presumed that this was due to the production of intermediates during the degradation of toluene, which were adsorbed on the surface of the catalyst. During the degradation of toluene, small molecules such as alcohols, carboxylic acids, and so on were produced and stay on the surface of the material and continue to decompose.

To investigate the degradation process of toluene during the reaction, in this study, after the catalytic ozonation experiment, we collected the produced gas and the organic matter adsorbed on the surface of $ZnFe_2O_4/\gamma$-$Al_2O_3$ catalyst. The experimental conditions were as follows: an initial toluene concentration of 600 mg $m^{-3}$, a temperature of 293 K, and a space velocity of 1000 $h^{-1}$. With these conditions, toluene had a sufficiently high conversion rate to produce enough intermediates for measurement. As shown in Fig. S11a, b and Table S6,† the $ZnFe_2O_4/\gamma$-$Al_2O_3$ catalyst revealed the main substances, including: toluene ($C_7H_8$), benzyl alcohol ($C_7H_8O$), benzaldehyde ($C_7H_6O$), benzyl methyl ether ($C_8H_{10}O$), benzaldehyde dimethyl acetal ($C_9H_{12}O_2$), acetic acid, phenylmethyl ester ($C_9H_{10}O_2$), benzyl ether ($C_{14}H_{14}O$), benzene ($C_6H_6$), cyclobutanone ($C_4H_6O$), propanedioic acid ($C_3H_4O_4$), ethyl hydrogen malonate ($C_5H_8O_4$), acetic acid ($C_2H_4O_2$), ethanol ($C_2H_6O$), methyl formate ($C_2H_4O_2$), and methanol ($CH_4O$). In the produced gas, there was only one carbonaceous material – carbon dioxide ($CO_2$). The difference between the main components of the produced gas and the organic matter adsorbed on the $ZnFe_2O_4/\gamma$-$Al_2O_3$ catalysts surface confirmed that most of the catalytic ozonation process took place on the $ZnFe_2O_4/\gamma$-$Al_2O_3$ catalyst's surface (including toluene and intermediates) in the case of the efficient removal of toluene.

Based on our analysis, GC-MS results and published studies,[11,12] the high concentration toluene catalytic ozonation routes using the $ZnFe_2O_4/\gamma$-$Al_2O_3$ catalyst with ambient temperature and pressure were proposed in Scheme 1. In general, the methyl group on the benzene ring in toluene was most easily oxidized, and the free radical can directly extract the H atom from the methyl group to be further converted into a benzyl group. The benzyl peroxy radicals can interact to form a tetraoxide, and the tetraoxide can be further decomposed by the Russell reaction. At the same time, benzyl radicals were directly oxidized to benzaldehyde and benzyl alcohol. At this stage, we suspected that benzoic acid would also be formed by the process of oxidizing benzaldehyde and benzyl alcohol. Subsequently, along with the ring-opening process of the benzene ring, a series of long-chain oxygen-containing small molecules and cyclobutanone were generated. These intermediates continued to be degraded by the catalytic ozonation on the catalyst surface. Among them, benzyl acetate was derived from the synthesis of acetic acid and benzyl alcohol. Finally, $CO_2$ and $H_2O$ were generated and discharged with the produced gas. From this analysis, we confirmed that the degradation of toluene was achieved by the adsorption and oxidation processes on the $ZnFe_2O_4/\gamma$-$Al_2O_3$ catalyst's surface. In order to further explore the carbon conversion pathways in this process, we also studied the effect of space velocity on the product. The experimental data were collated in Fig. S12.† With the increase of space velocity, not only the removal rate of toluene decreased, but the conversion rate of $CO_2$ also decreased significantly. When the space velocity was above 1500 $h^{-1}$, the $CO_2$

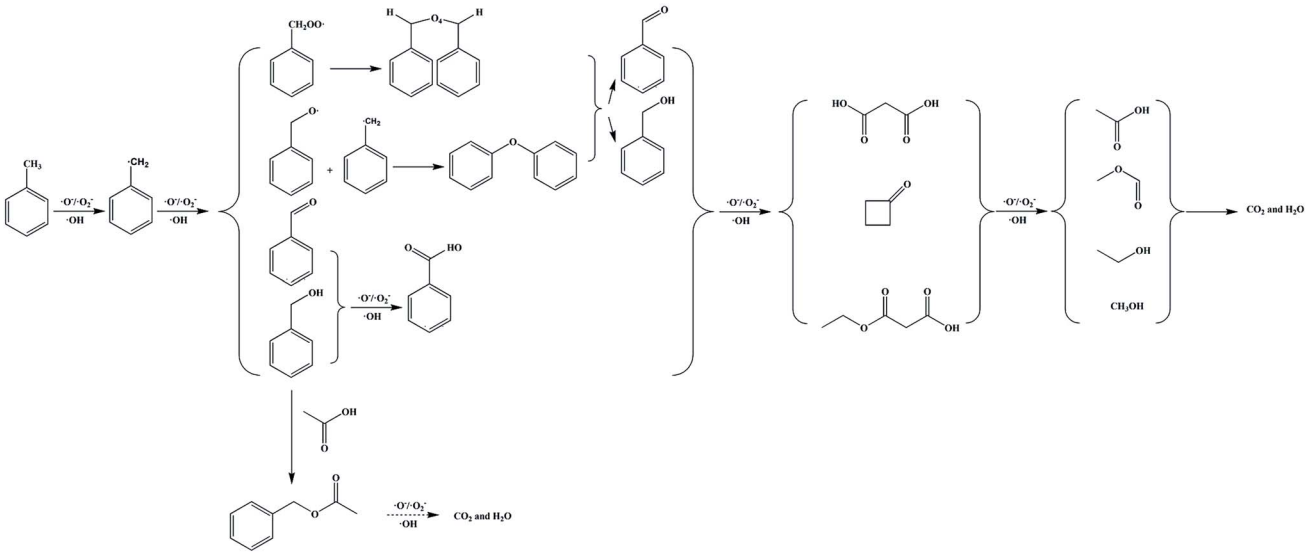


Scheme 1 Proposed toluene catalytic ozonation routes over catalysts. Note: this proposed mechanism was lack of the specific production process of water.

 

conversion rate is low. At this time, a large amount of by-products adhere to the catalyst surface, which affects the degradation rate of toluene. During the catalytic ozonation process, except for undegraded toluene and $CO_2$, almost no other products were discharged with the produced gas.

## Conclusion

Several high-purity $AFe_2O_4/\gamma\text{-}Al_2O_3$ (A = Zn, Co, Mn, Cu) catalysts with strong catalytic performance was prepared by hydrothermal synthesis. The performance of the catalyst was mainly attributed to the large number of surface oxygen vacancies, Lewis acid sites, Brønsted acid sites. The $ZnFe_2O_4/\gamma\text{-}Al_2O_3$ catalyst exhibited excellent and stable catalytic ozonation activity towards the degradation of toluene waste gas simulated at ambient temperature. The catalyst exhibited a strong catalytic efficiency, and the removal efficiency exceeds 99.8% under the optimal reaction conditions. The catalytic ozonation degradation pathway of toluene was identified using GC-MS. The methyl group on the benzene ring was preferentially attacked by the oxidizing substance, and then, the benzene ring was opened to form a series of small molecular groups, eventually generating $CO_2$ and $H_2O$. In addition, $\cdot O_2^-$ and $\cdot OH$ were identified as the main active substances in the catalytic ozonation degradation. More importantly, the developed catalyst demonstrated excellent reusability. This indicated that the catalyst might be a valuable candidate for the high concentrations of industrial toluene waste gas degradation.

## Conflicts of interest

There are no conflicts to declare.

## Acknowledgements

Sincere thanks are extended to the Natural Science Foundation of China (No. 21277020) for its financial contributions.

## Notes and references

1 J. Wang, Z. Ge and L. Pei, *Catal. Sci. Technol.*, 2019, **9**, 6681–6690.
2 W. Zhou, Z. Guan, M. Zhao and M. Li, *Chemosphere*, 2019, **226**, 766–773.
3 G. Y. Oh, Y. W. Ju and M. Y. Kim, *Sci. Total Environ.*, 2008, **393**(2–3), 341–347.
4 A. S. R. Castillo, S. Guiheneuf and R. L. Guevel, *J. Hazard. Mater.*, 2016, **307**, 221–230.
5 H. W. Ryu, M. Y. Song, J. S. Park, J. M. Kim and S. C. Jung, *Environ. Res.*, 2019, **172**, 649–657.
6 Y. Wang, L. Guo and M. Chen, *Catal. Sci. Technol.*, 2018, **8**, 459–471.
7 Y. Li, Z. Fan, J. Shi, Z. Liu and W. Shangguan, *Chem. Eng. J.*, 2014, **241**, 251–258.
8 L. Sivachandiran, F. Thevenet and P. Gravejat, *Chem. Eng. J.*, 2013, **214**, 17–26.
9 E. M. Drakou, M. Koutinas and I. Pantelides, *Int. Biodeterior. Biodegrad.*, 2015, **99**, 85–94.
10 P. Aken, P. Broeck and J. Degreve, *J. Cleaner Prod.*, 2017, **161**(10), 1432–1441.
11 Y. Shua, M. He, J. Ji, H. Huang and S. Liu, *J. Hazard. Mater.*, 2019, **364**, 770–779.
12 H. Valdés, V. A. Solar, E. H. Cabrera, A. F. Veloso and C. A. Zaror, *Chem. Eng. J.*, 2014, **244**, 117–127.
13 Z. Zhang, Z. Jiang and W. Shangguan, *Catal. Today*, 2016, **264**, 270–278.
14 C. W. Kwong and C. Y. H. Chao, *Environ. Sci. Technol.*, 2008, **42**(22), 8504–8509.
15 G. Oh, S. Y. Park, M. W. Seo, Y. K. Kim, H. W. Ra, J. Lee and S. J. Yoon, *Renew. Energy*, 2016, **86**, 841–847.
16 C. Lai, G. Huang, G. Zeng, D. Huang, L. Qin and M. Cheng, *Chemosphere*, 2015, **224**, 910–921.
17 M. S. Kamal, S. A. Razzak and M. M. Hossain, *Atmos. Environ.*, 2016, **140**, 117–134.
18 Y. Wang, Y. Xie, H. Sun, J. Xiao and H. Cao, *J. Hazard. Mater.*, 2016, **301**, 56–64.
19 Y. Sharma, N. Sharma and G. V. S. Rao, *Mater. Sci.*, 2008, **32**, 295–304.
20 D. Gao, Z. Shi, Y. Xu and J. Zhang, *Nanoscale Res. Lett.*, 2010, **5**, 1289.
21 J. Bennet, R. Tholkappiyan, K. Vishista and N. V. Jaya, *Appl. Surf. Sci.*, 2016, **383**, 113–125.
22 P. Zhang, I. Lo, D. O'Connor and S. Pehkonen, *J. Colloid Interface Sci.*, 2017, **508**, 39–48.
23 T. Fujii, F. M. F. de Groot, G. A. Sawatzky, F. C. Voogt, T. Hibma and K. Okada, *Phys. Rev. B: Condens. Matter Mater. Phys.*, 1999, **59**, 3195–3202.
24 Y. Lou, J. Ma, X. Cao, L. Wang, Q. Dai, Z. Zhao, Y. Cai, W. Zhan, Y. Guo, P. Hu, G. Lu and Y. Guo, *ACS Catal.*, 2014, **4**(11), 4143–4152.
25 J. Haetge, C. Suchomski and T. Brezesinski, *Inorg. Chem.*, 2010, **49**, 11619–11626.
26 Z. Xing, Z. Ju, J. Yang and H. Xu, *Nano Res.*, 2012, **5**, 477–485.
27 H. Einaga and S. Futamura, *Appl. Catal., B*, 2005, **60**(1–2), 49–55.
28 T. Gopi, G. Swetha, S. C. Shekar and C. Ramakrishna, *Catal. Commun.*, 2017, **92**, 51–55.
29 S. C. Kim and W. G. Shim, *Appl. Catal., B*, 2010, **98**(3–4), 180–185.
30 Y. Liao, M. Fu, L. Chen, J. Wu, B. Huang and D. Ye, *Catal. Today*, 2013, **216**, 220–228.
31 S. Liang, F. Teng, G. Bulgan and R. Zong, *J. Phys. Chem. C*, 2008, **112**, 5307–5315.
32 X. Wang, X. Wang, L. Lu, B. Wang, Z. Xu and Z. Xin, *Adv. Funct. Mater.*, 2018, **28**, 1–9.
33 X. Weng, P. Sun, Y. Long and Q. Meng, *Environ. Sci. Technol.*, 2017, **51**(14), 8057–8066.
34 D. R. Brown and C. N. Rhodes, *Catal. Lett.*, 1997, **45**(1–2), 35–40.
35 M. Piumetti, D. Fino and N. Russo, *Appl. Catal., B*, 2015, **163**, 277–287.
36 X. Ding, W. Ho, J. Shang and L. Zhang, *Appl. Catal., B*, 2016, **182**, 316–325.

37 J. Lu, X. Wei, Y. Chang and S. Tian, *J. Chem. Technol. Biotechnol.*, 2016, **91**(4), 985–993.
38 F. Zhang, C. Wei, Y. Hu and H. Wu, *Sep. Purif. Technol.*, 2015, **156**(2), 625–635.
39 Q. Dai, J. Wang and J. Chen, *Appl. Catal., B*, 2014, **144**, 686–693.
40 J. Ma, W. Ma, W. Song, C. Chen and Y. Tang, *Environ. Sci. Technol.*, 2006, **40**(2), 618–624.
41 H. Huang, X. Ye, W. Huang, J. Chen, Y. Xu and M. Wu, *Chem. Eng. J.*, 2015, **264**, 24–31.
42 F. Zhang, C. Wei, K. Wu, H. Zhou, Y. Hu and S. Preis, *Appl. Catal., A*, 2017, **547**, 60–68.
43 G. Zhu, J. Zhu, W. Jiang, Z. Zhang, J. Wang and Y. Zhu, *Appl. Catal., B*, 2017, **209**, 729–737.
44 J. Bing, C. Hu, Y. Nie and J. Qu, *Environ. Sci. Technol.*, 2015, **49**, 1690–1697.
45 L. Yang, C. Hu, Y. Nie and J. Qu, *Environ. Sci. Technol.*, 2009, **43**(7), 2525–2529.

 